
LONG SHORT-TERM MEMORY NETWORKS FOR PROTON DOSE CALCULATION IN HIGHLY HETEROGENEOUS TISSUES

A PREPRINT. UNDER REVIEW.

Ahmad Neishabouri

Department of Medical Physics in Radiation Oncology
German Cancer Research Center (DKFZ)
Im Neuenheimer Feld 280, D-69120
Heidelberg, Germany
a.neishabouri@dkfz-heidelberg.de

Niklas Wahl

Department of Medical Physics in Radiation Oncology
German Cancer Research Center (DKFZ)
Im Neuenheimer Feld 280, D-69120
Heidelberg, Germany
n.wahl@dkfz-heidelberg.de

Ulrich Köthe

Visual Learning Lab
Interdisciplinary Center for Scientific Computing (IWR)
University of Heidelberg
Im Neuenheimer Feld 205 D-69120
Heidelberg, Germany
ulrich.koethe@iwr.uni-heidelberg.de

Mark Bangert

Department of Medical Physics in Radiation Oncology
German Cancer Research Center (DKFZ)
Im Neuenheimer Feld 280, D-69120
Heidelberg, Germany
m.bangert@dkfz-heidelberg.de

ABSTRACT

A novel dose calculation approach was designed based on the application of LSTM network that processes the 3D patient/phantom geometry as a sequence of 2D computed tomography input slices yielding a corresponding sequence of 2D slices that forms the respective 3D dose distribution. LSTM networks can propagate information effectively in one direction, resulting in a model that can properly imitate the mechanisms of proton interaction in matter. The study is centered on predicting dose on a single pencil beam level, avoiding the averaging effects in treatment plans comprised of thousands pencil beams. Moreover, such approach allows straightforward integration into today's treatment planning systems' inverse planning optimization process. The ground truth training data was prepared with Monte Carlo simulations for both phantom and patient studies by simulating different pencil beams impinging from random gantry angles through the patient geometry. For model training, 10'000 Monte Carlo simulations were prepared for the phantom study, and 4'000 simulations were prepared for the patient study. The trained LSTM model was able to achieve a 99.29 % gamma-index pass rate ([0.5%, 1 mm]) accuracy on the set-aside test set for the phantom study, and a 99.33 % gamma-index pass rate ([0.5%, 2 mm]) for the set-aside test set for the patient study. These results were achieved for each pencil beam in 6-23 ms. The average Monte Carlo simulation run-time using Topas was 1160 s. The generalization of the model was verified by testing for 5 previously unseen lung cancer patients. LSTM networks are well suited for proton therapy dose calculation tasks. However, further work needs to be performed to generalize the proposed approach to clinical applications, primarily to be implemented for various energies, patient sites, and CT resolutions/scanners.

Keywords Radiation therapy, particle therapy, proton therapy, treatment planning, dose calculation, deep learning

1 Introduction

The spatial calculation of the radiation dose within the patient's body is a central component of computer-aided treatment planning in the general radiotherapy chain. Thereby, accuracy is key - only a precise dose estimate enables a meaningful, patient-specific assessment of the treatment plan before the onset of therapy [1, 2, 3, 4].

At the same time, requirements regarding the dose calculation speed keep rising. Real-time dose calculation for adaptive radiotherapy (ultimately during treatment) [5, 6, 7], massively repeated dose calculation for uncertainty quantification [8, 9, 10, 11, 12], and complex simulations for biological effectiveness [13, 14] are still too time-consuming for widespread clinical application.

For particle therapy, the trade-off between dose calculation speed and accuracy is defined by pencil beam algorithms on the one end and Monte Carlo algorithms on the other end. While pencil beam algorithms provide faster dose estimates, Monte Carlo algorithms require a higher computational load [15, 16]. At the same time, however, Monte Carlo algorithms clearly outperform pencil beam algorithms regarding accuracy in complex geometries [17, 18, 19].

Currently, state-of-the-art deep learning (DL) technology is making an impact at various stages in radiotherapy. This process is most notably in classical machine learning domains such as outcome analysis and image processing [20, 21, 22, 23, 24]. Academic studies investigating deep learning for dose calculation are limited, and they primarily investigate the feasibility of deep learning methods in photon therapy [25, 26, 27, 28]. Furthermore, considerations are restricted on training a 2D/3D model (e.g. U-Net [29]) on the accumulative dose distribution extracted from prior-planned patient data, which poses problems for an application within inverse planning and seamless integration into existing workflows. This holds also true for recent work demonstrating the feasibility of improving protons dose calculation accuracy from the pencil beam algorithms to the level of Monte Carlo simulations, by learning from the prior-planned patient plans [30].

In this manuscript, we introduce a novel dose calculation approach for proton therapy based on the application of long short-term memory (LSTM) networks [31], in an attempt to mimic the physics of proton interactions with matter in a single pencil beam level. We restrict this study to a minimal number of parameter dependence, and establish an end-to-end model that predicts the dose distribution based on the input CT. Therefore, the 3D proton dose distribution of a pencil beam within the patient is understood as a sequence of two-dimensional dose slices along the beam direction.

LSTM networks, unlike conventional feed-forward networks, have a hidden inner state enabling efficient processing of sequences of data and effective propagation of information along the sequence [32]. Currently, LSTM networks are applied highly successful for time-series data, e. g. stemming from speech or video [33, 34, 35, 36]. To the best of our knowledge, this is the first work to exploit ANNs, and specifically LSTM networks, to perform proton dose calculation.

The designed approach will be further motivated in the following section 2 along with details on our LSTM architecture and training process. Section 3 presents results from a dose calculation accuracy study on model geometries and real-world lung patient cases. The limitations of our study and general opportunities provided through LSTM network proton dose calculations are discussed in section 4, section 5 concludes the paper.

2 Material and methods

The elementary task underlying the dose calculation for an entire intensity modulated proton therapy treatment is the calculation of the dose of a single proton pencil beam. In this context, a pencil beam denotes a bunch of protons leaving the treatment nozzle with a reasonably confined momentum distribution, as determined by the beam shaping devices.

Consequently, our study focuses on considerations for individual pencil beams. This reduction was chosen to study the fundamental characteristics of LSTM network-based dose calculations without averaging effects in treatment plans comprised of thousands of pencil beams which may conceal important aspects regarding the accuracy of the physical dose deposition.

2.1 Conventional proton dose calculation

With conventional dose calculation approaches, the 3D dose distribution of a single pencil beam within the patient body \mathcal{D} is a function of the initial phase space (i., e., the initial position and momentum distribution) of the particles \mathcal{P} and the 3D patient geometry \mathcal{G} .

$$\mathcal{D} = f(\mathcal{P}, \mathcal{G}) \tag{1}$$

The patient geometry is usually determined with a computed tomography (CT) scan where the Hounsfield units (HU) get translated into material composition distributions for Monte Carlo algorithms with custom calibration curves. Based on samples from the initial phase space of the particles, Monte Carlo algorithms simulate the path of individual protons and the associated energy deposition within the patient, as determined by its interactions with the patient geometry. The final dose distribution is then given by the sum of the deposited energy of all simulated particles. While this approach

allows for highly precise dose estimates with sufficient histories being simulated, even in challenging geometries, the repeated simulation of individual particles is very time consuming.

In our study, the Monte Carlo dose calculations were carried out with the Topas (TOol for PArticle Simulation) wrapper [37] for Geant4 [38]. The initial particle energy was 104.25 MeV for all simulations providing a reasonable trade-off between a meaningful penetration depth and acceptable dose calculation as well as LSTM network training run-times during prototyping.

2.2 Neural networks for proton dose calculation

In order to train a neural network for proton dose calculations, it is necessary to learn a mapping from the 3D patient geometry \mathcal{G} and the initial particle phase space \mathcal{P} to the 3D dose distribution \mathcal{D} , as laid out in the previous section. In the following two subsections, we are going to explain (1) our parameterization of the proton dose calculation problem for a neural network and (2) the rationale underlying our network architecture.

2.2.1 Problem parameterization

In order to minimize the complexity of the training process for the neural network, we restrict the transformation to be learned for dose calculation to a single initial energy. Without the loss of generality (we can simply train one network per initial energy), this effectively reduces the space of possible dose calculation scenarios for the network and enables a denser sampling of the space of possible patient geometries and dose distributions.

The space of possible dose distributions can be further confined when switching from the patient coordinate system into the beam’s eye view coordinate system. Here, the dose deposition is always oriented along the z' -axis, as shown in figure 1. As the lateral extent and the particle range can be considered finite and is roughly known a priori for any given initial energy, it is further possible to perform a lateral and longitudinal clipping of the region of interest. In our case we use an isotropic resolution of 2 mm with $m = 15$ voxels in lateral direction and $l = 150$ voxels in longitudinal direction (for patient setup).

Further, we chose to perform the learning not on HU maps but on maps of the relative stopping power (RSP)¹ which are also used for conventional pencil beam algorithms [39, 17]. The RSP values are in turn translated into the respective water density for MC simulations.

In the described parameterization, we deal with a supervised regression problem that maps the geometry input data $\mathcal{G}_i \in \mathbb{R}_+^{l \times m \times m}$ to real-valued dose outputs $\mathcal{D}_i \in \mathbb{R}_+^{l \times m \times m}$.

2.2.2 Network architecture considerations

Due to the 3D nature of the problem, the intuitive implementation of a neural network for dose calculation is a 3D model such as a 3D U-net. These models have seen much attention recently with continuous advances in GPU hardware, and specifically GPU memory sizes, allowing processing of big data. However, the particle dose calculation problem exhibits a geometrical peculiarity that motivates a more specialized network architecture: dose deposition is almost exclusively taking place in a sequential *upstream-to-downstream* manner. I. e. the highly energetic protons predominantly travel along one direction with moderate lateral scatter until they stop. This characteristic behavior allows for a representation of the 3D input and output as a sequence of two-dimensional slices, as illustrated in figure 2.

Thence, the dose calculation problem has strong similarities to conventional video analysis in terms of spatio-temporal features. In action recognition tasks for instance, models have to extract spatial features of objects within each frame, and temporal features to interpret the movement of those objects. Simulating the protons traverse through matter, and consequently their dose deposition, is very similar to this task. It is completely determined by the upstream geometry, i. e., the geometry previously "seen" by the protons along their track through the patient. This implies causality from upstream to downstream within the 3D volume and it suggest a special role for regions in the input data that have high gradients in their RSP values (e. g. material interfaces to bones with high RSP and cavities with low RSP). Thereby, the effect of each heterogeneity on the dose deposition is most pronounced at the end of the proton range as demonstrated in figure 3. Consequently, any model to simulate dose deposition for particles needs to extract spatio-temporal features and precisely propagate the impact of heterogeneities along the particle tracks.

While recent studies [40, 41, 42] have shown that 3D-CNN models are capable of extracting spatio-temporal features through sequential data, consideration has to be taken with regard to the length of the sequences. In our application domain protons may have high ranges of more than 300 mm and consequently very high number of slices which may lead to issues with an adequate receptive field for detecting such long coherence. The 3D-CNN by design has the

¹The RSP denotes the range loss in the geometry relative to a water phantom.

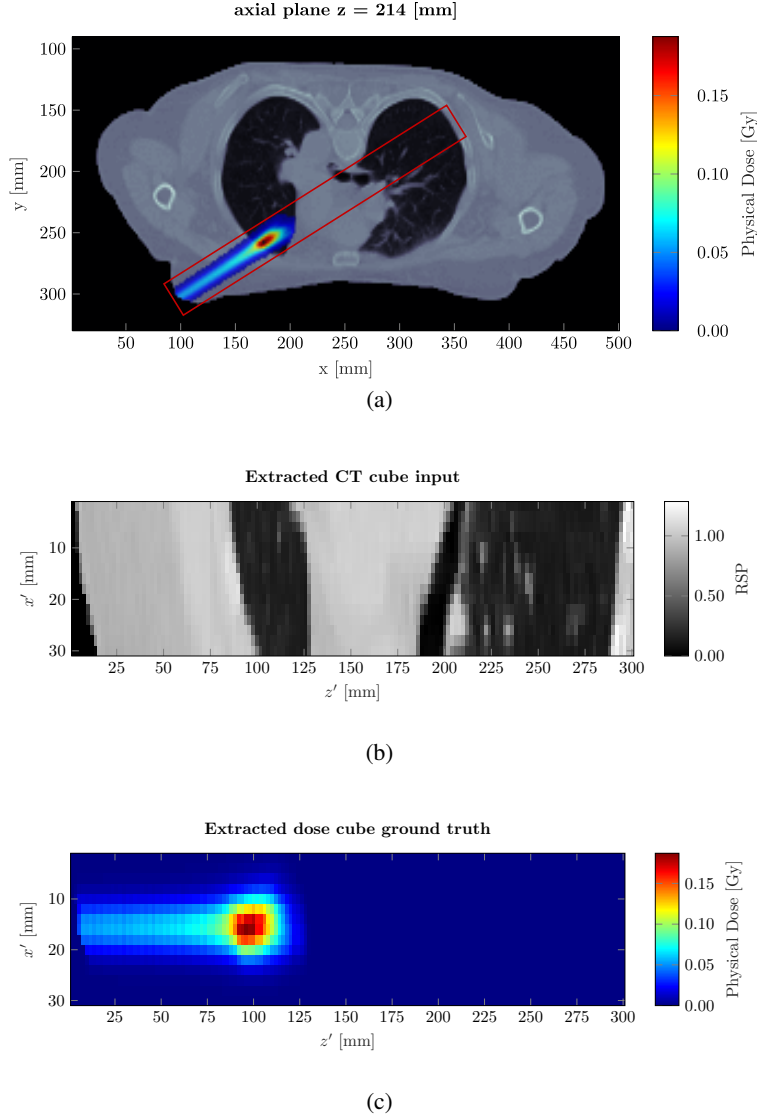


Figure 1: (a) Dose distribution of a single pencil beam with initial energy 104.25 MeV impinging from gantry angle 240° overlaying the patient CT. The clipping region is highlighted with a red box. (b) Respective CT slice and (c) dose distribution in beam's eye view coordinate system.

disadvantage of having high computational complexity and excessive memory usage [40]. In order to capture temporal coherence, the total number of parameters of 3D-CNNs will increase manifolds depending on the size of the temporal receptive field.

Processing sequences with long dependencies requires a model capable of passing information through the series. Recurrent Neural Networks (RNNs) with their hidden inner states, are capable of connecting many conventional one-input-to-one-output neural networks resulting in a model suitable to process on a many-input-to-many-output layouts. LSTM networks, an evolved version of simple RNNs, are capable of effectively transmitting relevant information through very long series thanks to their internal mechanism. Moreover, one directional LSTM models can fully adapt to the upstream-to-downstream propagation scheme of protons, eliminating dependencies between downstream to upstream resulting in a substantially reduced number of parameters for the model.

¹Note that this figure is illustrating the RNN/LSTM network in an *unfolded* fashion [43].

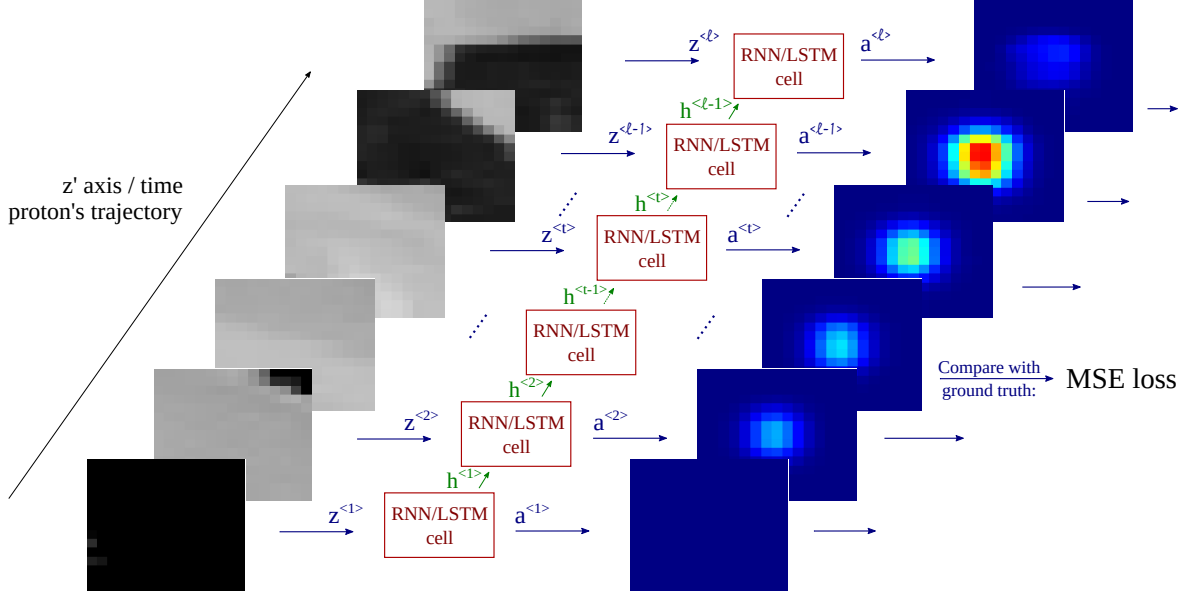


Figure 2: Sequential, spatio-temporal modeling of the proton dose calculation problem. each $m \times m$ slice of the input is flattened into a 1D input array $z^{<t>}$. Each input array is then passed to the RNN/LSTM¹ cell generating a hidden inner state $h^{<t>}$ and an output $a^{<t>}$. The hidden inner state is passed as an input information for subsequent slices (l slices in total), while the output is passed to a fully connected neural network back end to generate an $m \times m$ output slice. The output is then compared to the original ground truth by means of mean squared error loss.

2.2.3 LSTM networks

RNN models are distinguished by having a hidden internal state, enabling them to retain temporal information, similar to a memory. Considering our problem parameterization, depicted in figure 2 of having an input sequence $\{z_1, \dots, z_{t-1}, z_t, z_{t+1}, \dots, z_l\}$ and output sequence $\{a_1, \dots, a_{t-1}, a_t, a_{t+1}, \dots, a_l\}$ with $z_t = [z_1, \dots, z_{m^2}]$ and $a_t = [a_1, \dots, a_n]$, RNNs calculate a hidden inner state $h_t \in \mathbb{R}^K$ with K hidden units, and the output a_t via the following recurrence equations:

$$\begin{aligned} h_t &= f(W_{IH}z_t + W_{HH}h_{t-1} + b_H), \\ a_t &= f(W_{HO}h_t + b_O), \end{aligned} \quad (2)$$

where f denotes an element-wise non-linear activation function. W_{IH} , W_{HH} and W_{HO} are the input-to-hidden, hidden-to-hidden, and hidden-to-output weight matrices, respectively. b_H and b_O denote the hidden and output layer biases. The weight matrices and the biases are shared parameters that, given a properly converging training process during backpropagation, map relations between the input and output as desired. Simple RNNs, however, often suffer from the vanishing or exploding gradient problem during backpropagation with an increasing number of events in the input sequence. These problems arise due to the recursive derivative operations taken place along the sequence which may lead to very small or very big gradients, which in turn disrupt the training process and consequently restrict the RNN's capabilities to memorize long-term dependencies.

With the motivation to overcome the long-term dependency problem, LSTM networks were first introduced by Hochreiter et al. [31]. The key innovation in this context is a memory cell state c_t and associated update mechanisms via gates in addition to the hidden state h_t . In particular, the memory cell state has the capability of remaining unaltered, unless the three individually trained neural network layers, namely the *input*, *forget*, and *cell* gate determine to update the information within memory cell state. This mechanism inhibits repetitive multiplication of the gradients in the course of backpropagation algorithm and ensures efficient passage for relevant information through the sequence, as shown in figure 4. Finally, an additional neural network, the *output gate*, is trained to select the corresponding

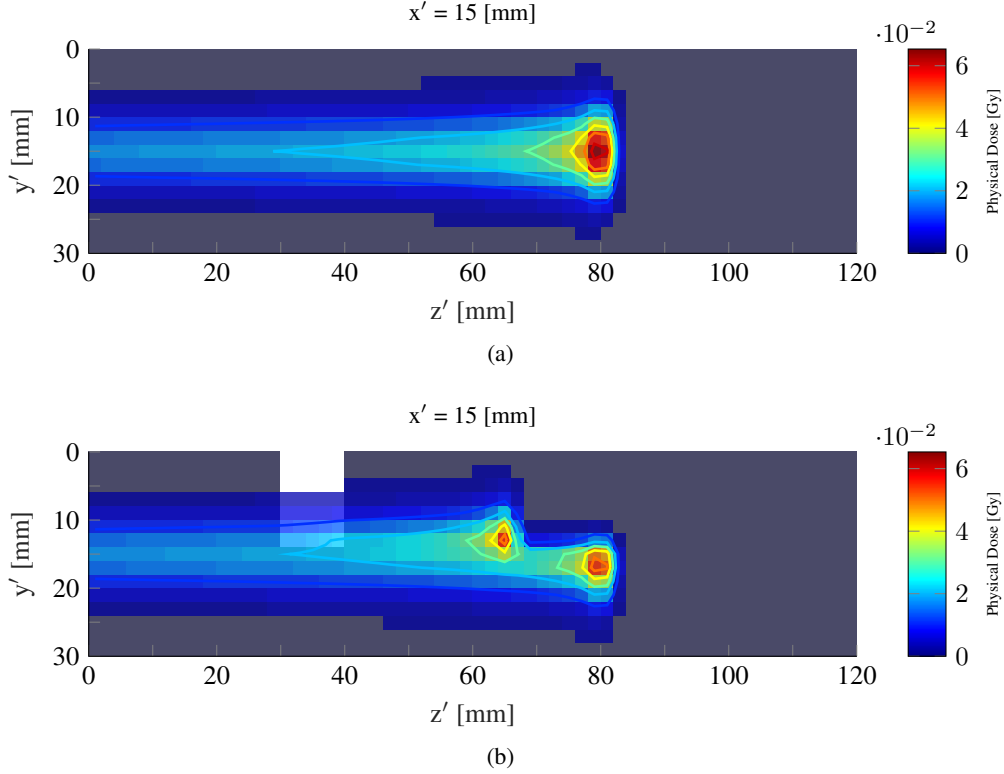


Figure 3: Effect of a heterogeneity on the shape of a pencil beam dose profile. The pencil beam is formed by 10^6 protons with an initial energy of 104.25 MeV passing through (a) water (1.0 RSP). (b) The cuboid heterogeneity (2.5 RSP) has 10 mm width in z' axis, 14 mm width in x' axis, and 1 mm distance to the center of the of proton beam. The effect of the cuboid mainly manifests in a bimodal Bragg peak region extending from ≈ 60 mm to 80 mm, i. e., 20mm after the heterogeneity.

information to output for the current time interval. Mathematically, each LSTM cell enclosing the mentioned gates can be described via the following equations

$$\begin{aligned}
 \mathbf{i}_t &= \sigma(\mathbf{W}_{i_1} \mathbf{z}_t + \mathbf{W}_{i_2} \mathbf{h}_{t-1} + \mathbf{b}_i) \\
 \mathbf{f}_t &= \sigma(\mathbf{W}_{f_1} \mathbf{z}_t + \mathbf{W}_{f_2} \mathbf{h}_{t-1} + \mathbf{b}_f) \\
 \mathbf{g}_t &= \tanh(\mathbf{W}_{g_1} \mathbf{z}_t + \mathbf{W}_{g_2} \mathbf{h}_{t-1} + \mathbf{b}_g) \\
 \mathbf{o}_t &= \sigma(\mathbf{W}_{o_1} \mathbf{z}_t + \mathbf{W}_{o_2} \mathbf{h}_{t-1} + \mathbf{b}_o) \\
 \mathbf{c}_t &= \mathbf{f}_t \odot \mathbf{c}_{t-1} + \mathbf{i}_t \odot \mathbf{g}_t \\
 \mathbf{h}_t &= \mathbf{o}_t \odot \tanh(\mathbf{c}_t),
 \end{aligned} \tag{3}$$

where \mathbf{W}_{ξ_1} , \mathbf{W}_{ξ_2} , \mathbf{b}_{ξ} , $\xi \in \{i, f, g, o\}$, are the input-to-hidden weight matrices, hidden-to-hidden weight matrices, and biases that jointly are the learnable parameters constituting the input, forget, cell, and output gates, respectively. σ is the Sigmoid function restricting the outputs to values between zero and one, ensuring a functionality analogous to gates. \odot denotes the element-wise Hadamard product. The gates regulate the error propagation in the training process, thereby preventing the vanishing and exploding of the derivatives. Many variants of the original LSTM [44, 45, 46] have been introduced so far, and this study is using the Pytorch¹ implementation of this architecture.

2.2.4 LSTM Training

Training of the network was carried out with an Adam optimizer [47], with a learning rate of 10^{-5} and a Mean Squared Error (MSE) loss function. The LSTM cells featured one layer with 1000 neurons as internal layer, followed by a fully

¹<https://pytorch.org/docs/stable/nn.html#lstm>

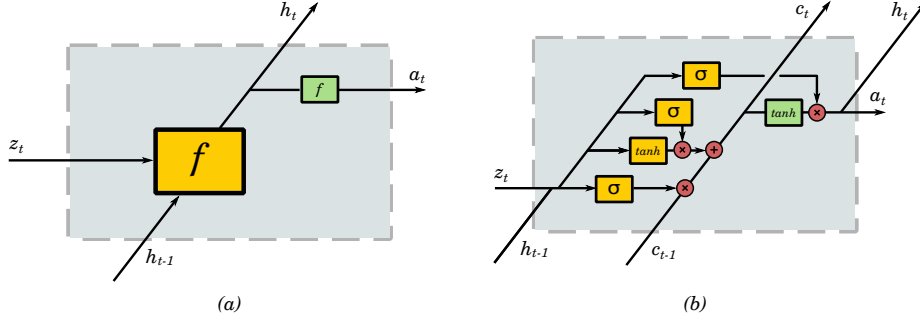


Figure 4: A schematic diagram of the internal module for (a) simple RNN cell and (b) for an LSTM cell.

connected neural network for the back end. The back end network features one hidden layer with 100 neurons and an output layer of m^2 to generate the slices. The dose cubes were normalized to have values in 0 to 1 range. Empirically, we found no improvement in test loss after about 100 epochs, and after that overfitting of the training set has been observed. Training of the network takes 3 to 4 hours for the patient data set described in the next section, with a Geforce GTX 970 GPU.

2.3 Dosimetric evaluation

2.3.1 Phantom cases

In order to study the performance of the proposed neural network dose calculation algorithms in an idealized setting, we first carried out simulations on phantom geometries featuring cuboid inhomogeneities of varying dimensions and densities placed randomly within a water phantom, as shown in figure 5. For this task, 2500 phantom samples were generated with corresponding dose distributions from TOPAS Monte Carlo simulations. This number was raised to 10 000 samples by augmenting rotated (90° angles) replicas of the cubes. 8000 samples were used as training set, and 2000 samples were used as test set. All the samples were simulated with $\sim 1.1 \times 10^6$ histories on average, resulting in less than 1% statistical uncertainty².

2.3.2 Lung cases

In order to study the performance of the proposed neural network dose calculation algorithms for real-world patient cases, we further considered dose calculation tasks on lung patient cases exhibiting highly pronounced inhomogeneities between normal tissue, lung tissue, and bony anatomy (rib cage & spine). For this task, 1000 lung case samples were generated with corresponding dose distributions from TOPAS Monte Carlo simulations (4000 after data augmentation). All samples stem from the same patient. Different geometric problems could be extracted from one patient by sampling the beam orientation in 5° steps from 0° to 355° in combination with isocenter position samples in 10 mm shifts spanning the lung along the z axis, as shown in Fig. 6. All the samples were simulated with 2.5×10^6 histories on average, ensuring a statistical uncertainty between 1% to 2%. 3200 samples were used as training set, 800 samples were used as test set. The original CT was downsampled to an isotropic 2 mm resolution. Consequently, the resulting HU map was transformed to an RSP map via HU look up tables yielding RSP values between 0 for vacuum and 2.5 for denser bone structures.

2.3.3 γ -index analysis

In order to compare 3D dose distributions, γ -analysis [48] was performed with a 0.5% distance-to-agreement and 1 mm dose difference criterion([0.5% , 1 mm] in short) for the water box phantom, and a [0.5% , 2 mm] criterion was chosen for the patient case. The γ -analysis represents the agreement of the two 3D dose distributions with a 3D numerical index γ , having values less than 1 for voxels which *pass* the agreement requirements, and values higher than 1 for voxels which *fail* the agreement requirements. Consequently, the γ -index pass rate demonstrates the percentage of voxels with $\gamma < 1$ out of all voxels with γ -index value higher than zero (we do not consider all voxels to avoid inclusion of passing voxels beyond the range of the dose).

²Uncertainty is calculated by dividing the highest standard deviation by the dose in that voxel

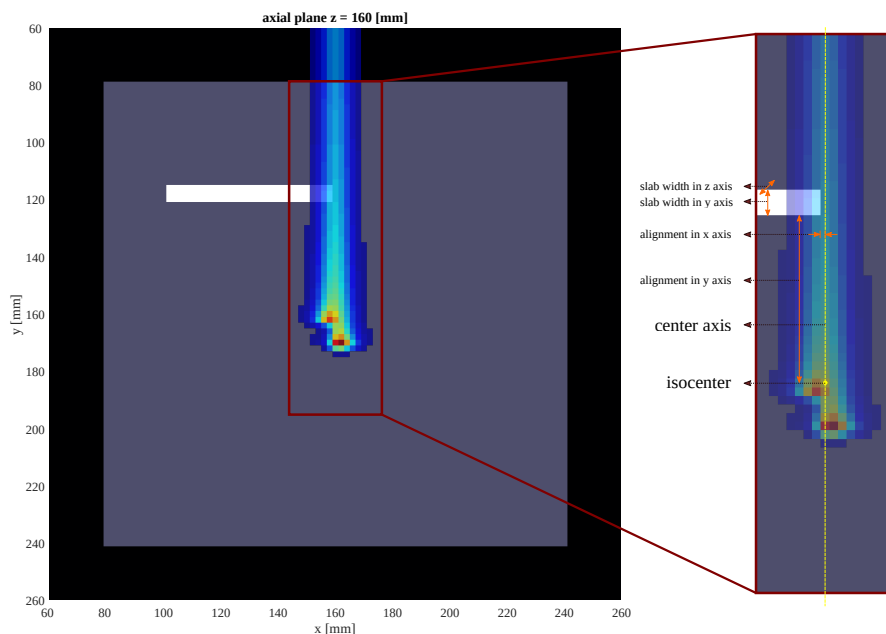


Figure 5: Phantom case setup; different geometric problems were generated by varying the slabs' dimensions in y and z axis, varying the alignment of the slab in x and y axis, and varying the density of both the water and the slab.

Unlike of dose difference maps, the γ -index provides a more holistic assessment of dose distribution differences, not only considering local dosimetric discrepancies but also spatial shifts (e. g. due to range offsets). Although computationally expensive, the γ -index pass rate reduces the discrepancy of two 3D dose distributions to a single number which facilitates the large scale comparisons needed for our study working with several thousand training and test samples.

3 Results

3.1 Phantom cases

The prepared dataset for the water box phantom was used for training of the simple RNN and the LSTM network. Figure 7 shows MSE loss plot for the training of both architectures for 100 epochs.

The performance of the two networks was further evaluated dosimetrically for the test set. Table 1 presents the outcome of the γ -analysis comparing the estimated dose from the networks with the ground truth MC calculations. While both networks seem generally suited for dose calculation with mean pass rates $>97.88\%$ (figure 3.1), the LSTM network outperforms the RNN by 1.5%. We have observed that differences between the LSTM network and RNN mainly originate from cases with pronounced heterogeneities as shown in Figure 9. In this example, the LSTM model demonstrates an evident improvement in comparison to the RNN model, which fails to predict the bimodal Bragg peak behind the density interface resulting in an ~ 8 percentage points increase in overall γ -index pass rate.

Table 1: γ -index analysis comparing the two trained models in water phantom case ([0.5%, 1mm]).

	mean	std	min	max
RNN	97.88	2.12	89.42	99.8
LSTM	99.29	0.8834	94.8	100

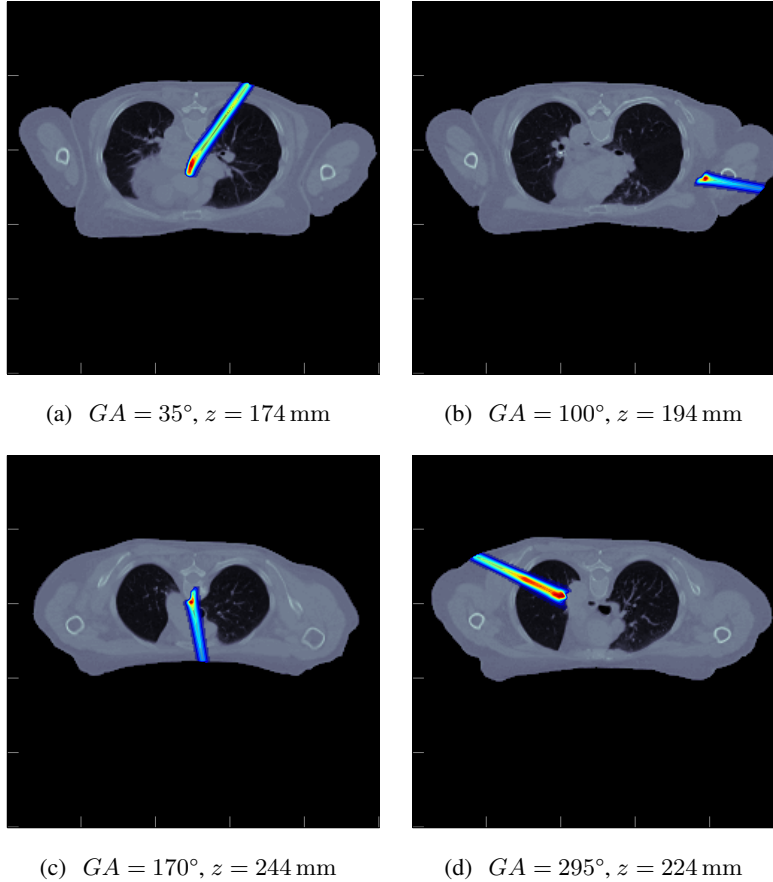


Figure 6: Lung case setup; generating different geometric problems for preparing training data set by varying the gantry angles (GA) and shifting the isocenter along the z axis.

3.2 Patient cases

Due to the promising results of the LSTM network on the phantom cases, especially those with pronounced heterogeneities, we also trained this architecture on the lung patient data set, as shown in Figure 10. Table 2 summarizes the outcome of the γ -analysis for the set-aside test set. Note that we also included a relaxed γ criterion of [0.5% , 2 mm] for the patient case. Due to the generation of the training and test set samples for the patient case by varying, among others, gantry angles, we have to deal with interpolation effects in the cube extraction that effect the γ -analysis at the previously used [0.5% , 1 mm] criterion.

Table 2: γ -index analysis comparing the trained LSTM model with MC calculations for the patient case

γ -analysis criteria	mean	std	min	max
[0.5% , 1 mm]	94.47	3.78	80.43	99.58
[0.5% , 2 mm]	99.33	0.92	94.91	100

Figure 11 shows the performance of the trained network on a representative test sample. In particular, we want to point out the capability of the trained network to deal with oblique gantry angles where voxels with vanishing density prior to entering the patient are successfully recognized and not confused with low density lung voxels lying within the patient. Furthermore, the LSTM network correctly predicts a smeared out Bragg peak without a distinct maximum at the end of the particles' range which is due to low density lung tissue at the location of the Bragg peak. Also the irregular shape of the distal fall-off which originates from inhomogeneities in the pencil beam track is qualitatively predicted by the network dose calculation algorithm. Additional samples are showcased in appendix A.

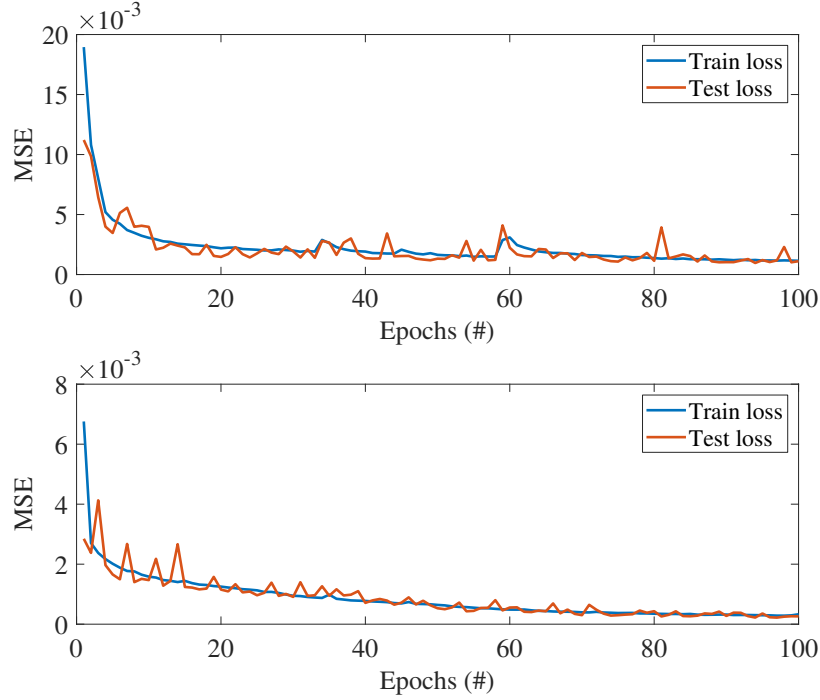


Figure 7: MSE loss function for training of the water box phantom data set for both the simple RNN architecture (top), and the LSTM architecture (bottom)

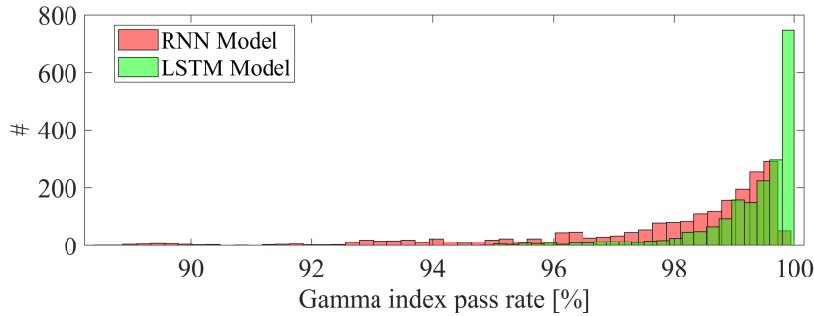


Figure 8: Comparison between the RNN and LSTM model γ -index pass rate distribution over all test cases.

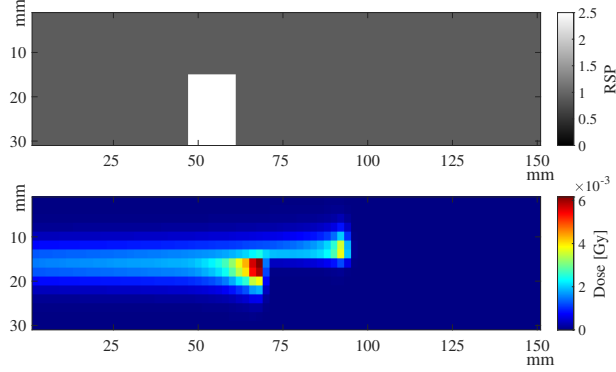
3.3 Model generalization

In order to assess the generalization of the LSTM dose calculation engine to previously unseen patients, i. e., data from other patients that was not considered during training, the performance of the network was evaluated on five additional lung cancer patients. For each patient, 200 pencil beams with randomly selected gantry angles and isocenter shifts were prepared, and the deposited dose was calculated using MC calculations. Table 3 lists the result of comparing the MC calculations with the network estimations using γ -index analysis.

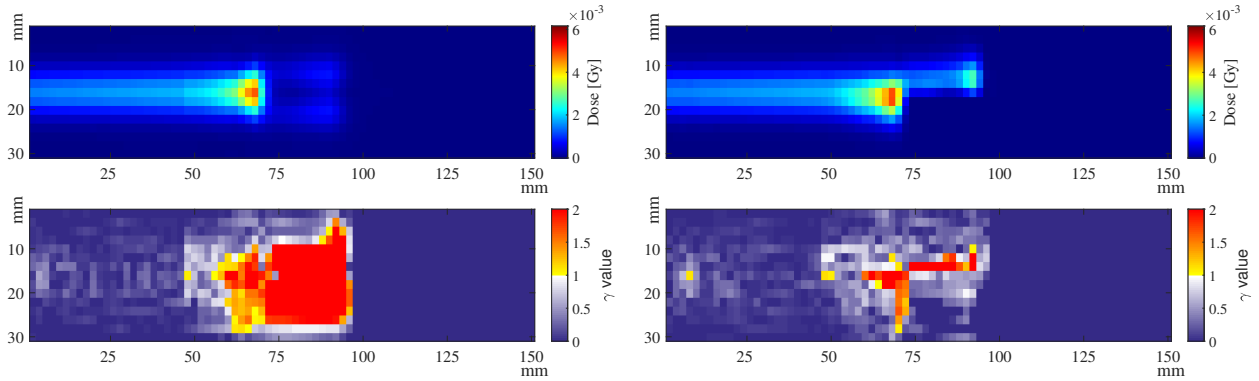
3.4 Run-times

In order to compare the run-times of incorporating the trained network as apposed to the MC algorithm, table 4 lists the average run-times for estimating the dose for the 5 above-mentioned patients for a single pencil beam, for both methods. The MC simulations were performed with Topas with a calculation node with 28 virtual CPUs on an Openstack² cluster. For the trained network, the run times were measured for two systems with different GPUs. Depending on the facilitated hardware, we measure average run-times of 6 ms to 23 ms for the LSTM approach. Note that this run-times included

²<https://www.openstack.org/>



(a) Input CT (top), ground truth MC calculation (bottom)



(b) RNN dose estimation (top), γ map (bottom) γ -index pass rate = 89.4 %

(c) LSTM dose estimation (top), γ map (bottom) γ -index pass rate = 97.1 %

Figure 9: Performance comparison of the (b) RNN and the (c) LSTM network with (a) ground truth MC calculation for a sample test data (104.25 MeV, with a 14 mm width slab and 2.5 RSP, γ -analysis criterion = [0.5 % , 1 mm])

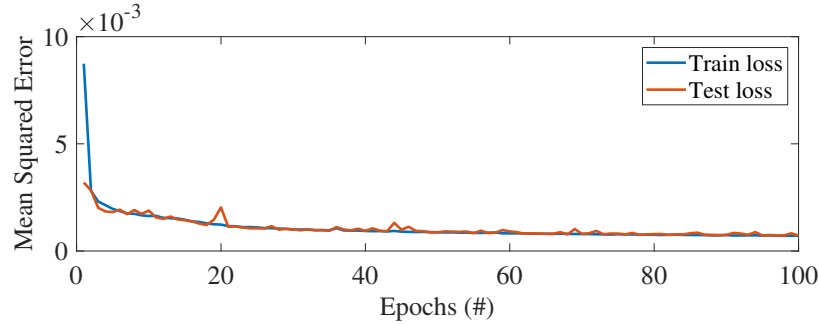


Figure 10: MSE loss function for training of the patient case data set with LSTM architecture

the time required to send the input CT cube for each pencil beam from CPU to GPU and vice versa for the yielded dose cube. However, in applications such as adaptive radiotherapy which requires repetitive online dose estimations, the input CT cubes can be prepared and sent to the GPU in advance. Consequently, the only relevant run-times would be the network feed forward, i.e. matrix multiplication operations run-times, reported to be 1.5 ms to 2.5 ms for the two facilitated hardware stacks. The average Topas run-time was 1160 s, performed with $\sim 2.5 \times 10^6$ histories on average (see section 2.3).

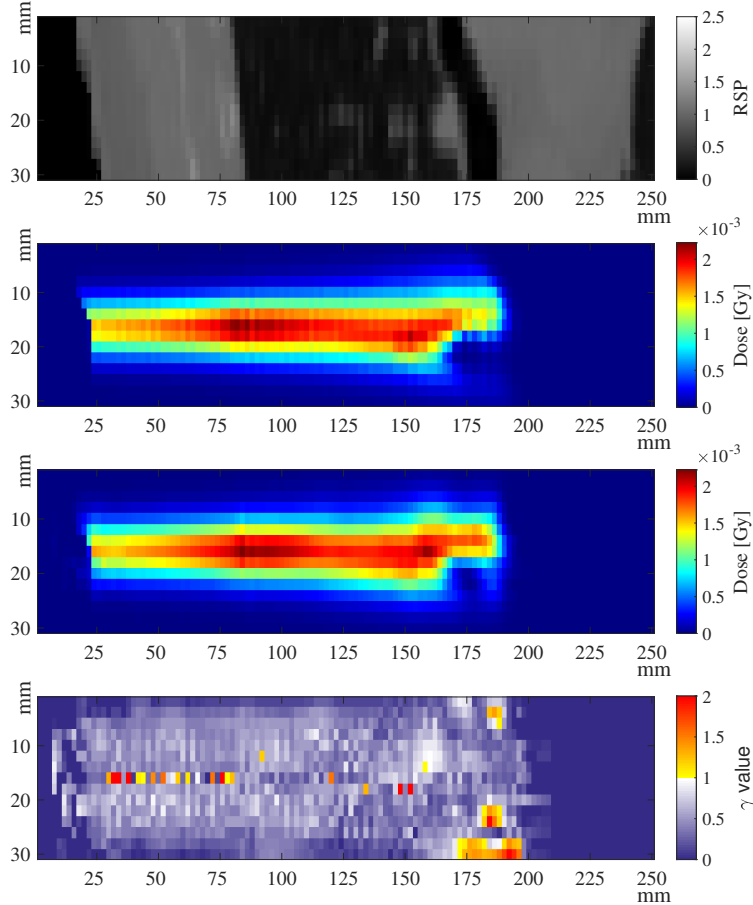


Figure 11: Dose estimation result for a sample test data (104.25 MeV). Starting from top is the input patient CT, the ground truth MC dose distribution, the estimated dose by the LSTM network, and the γ -index map ([0.5 % , 2 mm])

4 Discussion

In this paper, we have demonstrated the general feasibility of proton dose calculation based on an LSTM neural network. The LSTM network correctly models the proton dose deposition characteristics in the entrance, in the Bragg peak, and in the distal fall-off region - also in heterogeneous geometries. This covers particularly examples where conventional pencil beam algorithms fail, e. g. predicting a smooth bi-modal Bragg peak behind interfaces.

In comparison to RNN networks, LSTM networks proved particularly suited for this task, especially in heterogeneous geometries. This was also reflected in the training behavior, where the RNNs exhibited more pronounced fluctuations in MSE loss (compare figure 7).

Using phantom and lung patient cases, we have observed very good agreement for individual pencil beams with an initial energy of 104.25 MeV at run-times of 6 ms to 23 ms per pencil beam. While the γ -index pass rates for patients 1 to 3 was $>99\%$, the γ -index pass rates for patients 4 and 5 ranged between 96 % and 98 %. This slight decline was attributed to very low RSP values in lung which could not be discriminated against air volumes penetrated by the beam before entering the patient. This phenomenon originated from beam angles in the training set where the beam enters and exits the patient arms before impinging on the chest (see figures 12(a) and 15(d)). Even though these beam orientations would be probably excluded from clinical considerations, we decided to have them included as challenging test scenario for the networks.

Based on the approach to study dose calculation accuracy for an individual energy, we were able to show the generalization of our algorithm to patient cases that were not considered during LSTM training. In order to implement a dose calculation for an entire treatment plan, however, additional networks need to be trained for different energies. Alternatively, and conceptually more appealing, it may be possible to train a network that is able to generalize also over different initial energies.

Table 3: γ -index analysis on 5 different lung cancer patients

	mean	std	min	max
Patient 0 ¹	99.33	0.92	94.91	100
Patient 1	99.10	0.93	93.01	99.99
Patient 2	99.01	1.03	94.96	100
Patient 3	99.15	1.00	94.27	100
Patient 4 ²	97.94	2.27	85.07	100
Patient 5 ²	96.34	4.09	75.79	99.96

¹Network has been trained on this patient.

²Patients with very low RSP values in lung (further discussed in section 4)

Table 4: run-time comparison of the MC calculation vs. ANN predictions. Run times reported in parenthesis considers purely the network feed forward time consumption and does not count the time required to send each input/output from CPU to GPU and vice versa

	MC ¹	ANN ²	ANN ³
Average run time (s)	1159.5	0.023 (0.0025)	0.006 (0.0015)

¹28 VCPUs, 64 Gb RAM

¹Intel Core i7-6700 3.4 GHz - Nvidia GTX 970 - 64 Gb RAM

¹Intel Xeon W-2135 3.7 GHz - Nvidia Quadro RTX 6000 - 64 Gb RAM

Of course, the run time benefits of several orders of magnitude over MC simulations as shown in table 4 will not manifest in the same way for clinical treatment plans comprised of several thousands of pencil beams. Here, MC simulations can save substantially because the geometry will only be initialized once for the entire simulation. Furthermore it will be possible to reduce the number of histories per pencil beam to achieve sufficient statistical certainty over the entire treatment plan for a simple dose recalculation. For the computation of a dose influence matrix which is needed for dose optimization, however, the MC runtime reductions will be more moderate. On the other side, it will be possible to further accelerate LSTM-based dose calculation through dedicated deep learning hardware and leveraging the embarrassingly parallel nature of the problem. And, as previously indicated, the transfer times between CPU and GPU will only be necessary once per patient for LSTM network dose calculations. In our case this made up 75 % of the run time for the faster GPU hardware.

Moreover, this study was concentrated on the ability to estimate dose in heterogeneous geometries, and no effort was made in improving the model efficiency. In this regard, there exist various model compression techniques, e.g. pruning, quantization, and tensor decomposition methods (achieving low-rank structures in the weight matrices) [49, 50, 51], which can lower the number of parameters in fully connected layers substantially [52, 53]. The efficiency of the model can be further enhanced through fine-tuning of the model architecture. This study parameterized the size in longitudinal direction as a fixed hyper-parameter (parameter l , see section 2.2.1). While the range of mono-energetic protons are more or less fixed in a homogeneous geometry, it can vary substantially when they travel through wide cavities such as the Lung. This issue coerces us to train the model with very long sequences, to encompass all the potential pencil beam ranges. However, the LSTM models can be designed in what is referred to as *sequence to sequence learning*, which can accept a variable length input and outcome with a variable length output, incorporated effectively in Machine Translation problems [54]. Utilization of such a model can restrict the number of matrix multiplication operations accustomed to the plan, resulting in even faster estimations. In a different approach, one could also incorporate Autoencoders [55], as a back-end to the model, compressing the input CT to a latent feature space, leading to a reduction in number of input parameters.

The proposed dose estimation approach has not been exploited so far to the best of our knowledge, and we intend to explore this approach in many aspects. We see possible applications in photon dose calculation as well as in heavier ions (Carbon, Oxygen, Helium) dose calculation in an attempt to estimate biologically effective dose distributions.

5 Conclusion

In this paper, we have investigated the role of two different neural network architectures for proton dose calculation, i. e., an RNN and an LSTM network. For individual pencil beams on varying heterogeneous phantom geometries, the average γ -index pass rate ([0.5 % , 1 mm]) was 97.9 % for the RNN and 99.3 % for the LSTM network. The LSTM network was further evaluated on a highly heterogeneous lung case where we observed an average γ -index pass rate of 99.3 % ([0.5 % , 2 mm]). Average LSTM network run-times ranged between 6 ms to 23 ms.

Our results indicate that LSTM networks are well suited for particle therapy dose calculation tasks.

6 Acknowledgements

The authors thank Lucas Burigo for providing the TOPAS Monte Carlo interface for matRad.

References

- [1] Wayne Newhauser, Nicholas Koch, Stephen Hummel, Matthias Ziegler, and Uwe Titt. Monte carlo simulations of a nozzle for the treatment of ocular tumours with high-energy proton beams. *Physics in Medicine and Biology*, 50(22):5229–5249, October 2005. doi: 10.1088/0031-9155/50/22/002. URL <https://doi.org/10.1088/0031-9155/50/22/002>.
- [2] Wayne Newhauser, Jonas Fontenot, Yuanshui Zheng, Jerimy Polf, Uwe Titt, Nicholas Koch, Xiaodong Zhang, and Radhe Mohan. Monte carlo simulations for configuring and testing an analytical proton dose-calculation algorithm. *Physics in Medicine and Biology*, 52(15):4569–4584, July 2007. doi: 10.1088/0031-9155/52/15/014. URL <https://doi.org/10.1088/0031-9155/52/15/014>.
- [3] J Bauer, F Sommerer, A Mairani, D Unholtz, R Farook, J Handrack, K Frey, T Marcelos, T Tessonnier, S Ecker, B Ackermann, M Ellerbrock, J Debus, and K Parodi. Integration and evaluation of automated monte carlo simulations in the clinical practice of scanned proton and carbon ion beam therapy. *Physics in Medicine and Biology*, 59(16):4635–4659, July 2014. doi: 10.1088/0031-9155/59/16/4635. URL <https://doi.org/10.1088/0031-9155/59/16/4635>.
- [4] Stewart Mein, Benedikt Kopp, Thomas Tessonnier, Benjamin Ackermann, Swantje Ecker, Julia Bauer, Kyungdon Choi, Giulia Aricò, Alfredo Ferrari, Thomas Haberer, Jürgen Debus, Amir Abdollahi, and Andrea Mairani. Dosimetric validation of Monte Carlo and analytical dose engines with raster-scanning 1H, 4He, 12C, and 16O ion-beams using an anthropomorphic phantom. *Physica Medica*, 64(July):123–131, 2019. ISSN 1724191X. doi: 10.1016/j.ejmp.2019.07.001. URL <https://doi.org/10.1016/j.ejmp.2019.07.001>.
- [5] Stewart Mein, Kyungdon Choi, Benedikt Kopp, Thomas Tessonnier, Julia Bauer, Alfredo Ferrari, Thomas Haberer, Jürgen Debus, Amir Abdollahi, and Andrea Mairani. Fast robust dose calculation on GPU for high-precision 1H, 4He, 12C and 16O ion therapy: the FRoG platform. *Scientific Reports*, 8(1):1–12, 2018. ISSN 20452322. doi: 10.1038/s41598-018-33194-4.
- [6] Xun Jia, Jan Schümann, Harald Paganetti, and Steve B Jiang. GPU-based fast Monte Carlo dose calculation for proton therapy. 2012. doi: 10.1088/0031-9155/57/23/7783.
- [7] Yuhe Wang, Thomas R Mazur, Justin C Park, Deshan Yang, Sasa Mutic, and Harold Li. Development of a fast Monte Carlo dose calculation system for online adaptive radiation therapy quality assurance. *Physics in Medicine & Biology Institute of Physics and Engineering in Medicine*, 62:4970–4990, 2017. doi: 10.1088/1361-6560/aa6e38. URL <https://doi.org/10.1088/1361-6560/aa6e38>.
- [8] Jan Unkelbach, Thomas Bortfeld, Benjamin C. Martin, and Martin Soukup. Reducing the sensitivity of IMPT treatment plans to setup errors and range uncertainties via probabilistic treatment planning. *Medical Physics*, 36(1):149–163, dec 2008. ISSN 00942405. doi: 10.1118/1.3021139. URL <http://doi.wiley.com/10.1118/1.3021139>.
- [9] Aafke C. Kraan, Steven van de Water, David N. Teguh, Abraham Al-Mamgani, Tom Madden, Hanne M. Kooy, Ben J.M. Heijmen, and Mischa S. Hoogeman. Dose uncertainties in IMPT for oropharyngeal cancer in the presence of anatomical, range, and setup errors. *International Journal of Radiation Oncology, Biology, Physics*, 87(5):888–896, December 2013. doi: 10.1016/j.ijrobp.2013.09.014. URL <https://doi.org/10.1016/j.ijrobp.2013.09.014>.
- [10] Peter C. Park, Joey P. Cheung, X. Ronald Zhu, Andrew K. Lee, Narayan Sahoo, Susan L. Tucker, Wei Liu, Heng Li, Radhe Mohan, Laurence E. Court, and Lei Dong. Statistical assessment of proton treatment plans under setup

- and range uncertainties. *International Journal of Radiation Oncology, Biology, Physics*, 86(5):1007–1013, August 2013. doi: 10.1016/j.ijrobp.2013.04.009. URL <https://doi.org/10.1016/j.ijrobp.2013.04.009>.
- [11] Mark Bangert, Philipp Hennig, and Uwe Oelfke. Analytical probabilistic modeling for radiation therapy treatment planning. *Physics in Medicine and Biology*, 58(16):5401–5419, jul 2013. doi: 10.1088/0031-9155/58/16/5401. URL <https://doi.org/10.1088/0031-9155/58/16/5401>.
- [12] N Wahl, P Hennig, H P Wieser, and M Bangert. Efficiency of analytical and sampling-based uncertainty propagation in intensity-modulated proton therapy. *Physics in Medicine & Biology*, 62(14):5790–5807, June 2017. doi: 10.1088/1361-6560/aa6ec5. URL <https://doi.org/10.1088/1361-6560/aa6ec5>.
- [13] A Mairani, T T Böhlen, A Schiavi, T Tessonier, S Molinelli, S Brons, G Battistoni, K Parodi, and V Patera. A Monte Carlo-based treatment planning tool for proton therapy. *MEDICINE AND BIOLOGY Phys. Med. Biol*, 58: 2471–2490, 2013. doi: 10.1088/0031-9155/58/8/2471.
- [14] H P Wieser, P Hennig, N Wahl, and M Bangert. Analytical probabilistic modeling of {RBE}-weighted dose for ion therapy. *Physics in Medicine & Biology*, 62(23):8959–8982, nov 2017a. doi: 10.1088/1361-6560/aa915d. URL <https://doi.org/10.1088/1361-6560/aa915d>.
- [15] Matthias Fippel and Martin Soukup. A Monte Carlo dose calculation algorithm for proton therapy. *Medical Physics*, 31(8):2263–2273, jul 2004. ISSN 00942405. doi: 10.1118/1.1769631. URL <http://doi.wiley.com/10.1118/1.1769631>.
- [16] Hanitra Szymanowski and Uwe Oelfke. Two-dimensional pencil beam scaling: an improved proton dose algorithm for heterogeneous media. Technical report, 2002.
- [17] Barbara Schaffner, Eros Pedroni, and Antony Lomax. Dose calculation models for proton treatment planning using a dynamic beam delivery system: an attempt to include density heterogeneity effects in the analytical dose calculation. Technical report, 1999. URL <http://iopscience.iop.org/article/10.1088/0031-9155/44/1/004/pdf>.
- [18] Martin Soukup, Matthias Fippel, and Markus Alber. A pencil beam algorithm for intensity modulated proton therapy derived from Monte Carlo simulations. *Physics in Medicine and Biology*, 50(21):5089–5104, nov 2005. doi: 10.1088/0031-9155/50/21/010. URL <http://stacks.iop.org/0031-9155/50/i=21/a=010?key=crossref.d26e45f94e710de832fca244a5dcd17b>.
- [19] Paige A Taylor, Stephen F Kry, and David S Followill. Pencil Beam Algorithms Are Unsuitable for Proton Dose Calculations in Lung. *International Journal of Radiation Oncology { \textbullet } Biology { \textbullet } Physics*, 99(3):750–756, nov 2017. ISSN 0360-3016. doi: 10.1016/j.ijrobp.2017.06.003. URL <https://doi.org/10.1016/j.ijrobp.2017.06.003>.
- [20] Sarah L Gulliford, Steve Webb, Carl G Rowbottom, David W Corne, and David P Dearnaley. Use of artificial neural networks to predict biological outcomes for patients receiving radical radiotherapy of the prostate. *Radiotherapy and oncology*, 71(1):3–12, 2004.
- [21] Shupeng Chen, An Qin, Dingyi Zhou, and Di Yan. U-net-generated synthetic ct images for magnetic resonance imaging-only prostate intensity-modulated radiation therapy treatment planning. *Medical physics*, 45(12):5659–5665, 2018.
- [22] Dong Nie, Xiaohuan Cao, Yaozong Gao, Li Wang, and Dinggang Shen. Estimating ct image from mri data using 3d fully convolutional networks. In *Deep Learning and Data Labeling for Medical Applications*, pages 170–178. Springer, 2016.
- [23] Khosro Bahrami, Feng Shi, Islem Rekik, Yaozong Gao, and Dinggang Shen. 7t-guided super-resolution of 3t mri. *Medical physics*, 44(5):1661–1677, 2017.
- [24] Hubert S. Gabryś, Florian Buettner, Florian Sterzing, Henrik Hauswald, and Mark Bangert. Design and selection of machine learning methods using radiomics and dosiomics for normal tissue complication probability modeling of xerostomia. *Frontiers in Oncology*, 8:35, 2018. ISSN 2234-943X. doi: 10.3389/fonc.2018.00035. URL <https://www.frontiersin.org/article/10.3389/fonc.2018.00035>.
- [25] Dan Nguyen, Troy Long, Xun Jia, Weiguo Lu, Xuejun Gu, Zohaib Iqbal, and Steve Jiang. A feasibility study for predicting optimal radiation therapy dose distributions of prostate cancer patients from patient anatomy using deep learning. *Scientific Reports*, 9(1):1–10, dec 2019. ISSN 20452322. doi: 10.1038/s41598-018-37741-x.
- [26] C Kontaxis, G H Bol, J J W Lagendijk, and B W Raaymakers. DeepDose: Towards a fast dose calculation engine for radiation therapy using deep learning. *Physics in Medicine & Biology*, 65(7):75013, apr 2020. doi: 10.1088/1361-6560/ab7630. URL <https://doi.org/10.1088/1361-6560/ab7630>.

- [27] Rafid Mahmood, Aaron Babier, Andrea McNiven, Adam Diamant, and Timothy C Y Chan. Automated Treatment Planning in Radiation Therapy using Generative Adversarial Networks. In Finale Doshi-Velez, Jim Fackler, Ken Jung, David Kale, Rajesh Ranganath, Byron Wallace, and Jenna Wiens, editors, *Proceedings of the 3rd Machine Learning for Healthcare Conference*, volume 85 of *Proceedings of Machine Learning Research*, pages 484–499, Palo Alto, California, 2018. PMLR. URL <http://proceedings.mlr.press/v85/mahmood18a.html>.
- [28] Vasant Kearney, Jason W Chan, Samuel Haaf, Martina Descovich, and Timothy D Solberg. DoseNet: a volumetric dose prediction algorithm using 3D fully-convolutional neural networks. *Physics in Medicine & Biology*, 63(23):235022, 2018. doi: 10.1088/1361-6560/aaef74. URL <https://doi.org/10.1088/1361-6560/aaef74>.
- [29] Olaf Ronneberger, Philipp Fischer, and Thomas Brox. U-Net: Convolutional Networks for Biomedical Image Segmentation. In Nassir Navab, Joachim Hornegger, William M Wells, and Alejandro F Frangi, editors, *Medical Image Computing and Computer-Assisted Intervention – MICCAI 2015*, pages 234–241, Cham, 2015. Springer International Publishing. ISBN 978-3-319-24574-4.
- [30] Chao Wu, Dan Nguyen, Yixun Xing, Ana Barragan Montero, Jan Schuemann, Haijiao Shang, Yuehu Pu, Steve Jiang, and Steve Edu Jiang@utsouthwestern. Improving Proton Dose Calculation Accuracy by Using Deep Learning. Technical report.
- [31] Sepp Hochreiter and J J Urgen Schmidhuber. LONG SHORT-TERM MEMORY. Technical Report 8, 1997. URL <http://www7.informatik.tu-muenchen.de/~hochreith><http://www.idsia.ch/~juergen>.
- [32] Ilya Sutskever, Oriol Vinyals, and Quoc V. Le. Sequence to sequence learning with neural networks. In *Proceedings of the 27th International Conference on Neural Information Processing Systems - Volume 2, NIPS'14*, page 3104–3112, Cambridge, MA, USA, 2014a. MIT Press.
- [33] Alex Graves and Navdeep Jaitly. Towards end-to-end speech recognition with recurrent neural networks. In *Proceedings of the 31st International Conference on International Conference on Machine Learning - Volume 32, ICML'14*, page II–1764–II–1772. JMLR.org, 2014.
- [34] Jeff Donahue, Lisa Anne Hendricks, Marcus Rohrbach, Subhashini Venugopalan, Sergio Guadarrama, Kate Saenko, and Trevor Darrell. Long-term Recurrent Convolutional Networks for Visual Recognition and Description. Technical report. URL <http://jeffdonahue.com/lrcn/>.
- [35] Joe Yue-Hei Ng, Matthew Hausknecht, Sudheendra Vijayanarasimhan, Oriol Vinyals, Rajat Monga, and George Toderici. Beyond short snippets: Deep networks for video classification, 2015.
- [36] Will Kay, Joao Carreira, Karen Simonyan, Brian Zhang, Chloe Hillier, Sudheendra Vijayanarasimhan, Fabio Viola, Tim Green, Trevor Back, Paul Natsev, Mustafa Suleyman, and Andrew Zisserman. The kinetics human action video dataset, 2017.
- [37] J. Perl, J. Shin, J. Schümann, B. Faddegon, and H. Paganetti. TOPAS: An innovative proton Monte Carlo platform for research and clinical applications. *Medical Physics*, 39(11):6818–6837, oct 2012. ISSN 00942405. doi: 10.1118/1.4758060. URL <http://doi.wiley.com/10.1118/1.4758060>.
- [38] S. Agostinelli et al. GEANT4: A Simulation toolkit. *Nucl. Instrum. Meth. A*, 506:250–303, 2003. doi: 10.1016/S0168-9002(03)01368-8.
- [39] Hans-Peter Wieser, Eduardo Cisternas, Niklas Wahl, Silke Ulrich, Alexander Stadler, Henning Mescher, Lucas-Raphael Müller, Thomas Klinge, Hubert Gabrys, Lucas Burigo, Andrea Mairani, Swantje Ecker, Benjamin Ackermann, Malte Ellerbrock, Katia Parodi, Oliver Jäkel, and Mark Bangert. Development of the open-source dose calculation and optimization toolkit matRad. *Medical Physics*, 44(6):2556–2568, jun 2017b. doi: 10.1002/mp.12251. URL <http://doi.wiley.com/10.1002/mp.12251>.
- [40] Dongyi Kim, Hyeon Cho, Hochul Shin, Soo Chul Lim, and Wonjun Hwang. An efficient three-dimensional convolutional neural network for inferring physical interaction force from video. *Sensors (Switzerland)*, 19(16), aug 2019. ISSN 14248220. doi: 10.3390/s19163579.
- [41] Rui Hou, Chen Chen, and Mubarak Shah. An End-to-end 3D Convolutional Neural Network for Action Detection and Segmentation in Videos. Technical report.
- [42] Soo Ye, Kim Kaist, Jeongyeon Lim, and Taeyoung Na. 3DSRnet: Video Super-resolution using 3D Convolutional Neural Networks. Technical report.
- [43] Yann LeCun, Yoshua Bengio, and Geoffrey Hinton. Deep learning. *Nature*, 521(7553):436–444, May 2015. doi: 10.1038/nature14539. URL <https://doi.org/10.1038/nature14539>.
- [44] Alex Graves and Jürgen Schmidhuber. Framewise phoneme classification with bidirectional LSTM and other neural network architectures. *Neural Networks*, 18(5-6):602–610, July 2005. doi: 10.1016/j.neunet.2005.06.042. URL <https://doi.org/10.1016/j.neunet.2005.06.042>.

- [45] Felix A. Gers, Jürgen A. Schmidhuber, and Fred A. Cummins. Learning to forget: Continual prediction with lstm. *Neural Comput.*, 12(10):2451–2471, October 2000. ISSN 0899-7667. doi: 10.1162/089976600300015015. URL <https://doi.org/10.1162/089976600300015015>.
- [46] Felix A. Gers and Jürgen Schmidhuber. Recurrent nets that time and count. *Proceedings of the IEEE-INNS-ENNS International Joint Conference on Neural Networks. IJCNN 2000. Neural Computing: New Challenges and Perspectives for the New Millennium*, 3:189–194 vol.3, 2000.
- [47] Diederik P. Kingma and Jimmy Ba. Adam: A method for stochastic optimization, 2014.
- [48] Daniel A Low, William B Harms, Sasa Mutic, and James A Purdy. A technique for the quantitative evaluation of dose distributions. Technical report, 1998. URL <https://aapm.onlinelibrary.wiley.com/doi/pdf/10.1118/1.598248>.
- [49] Artem M. Grachev, Dmitry I. Ignatov, and Andrey V. Savchenko. Compression of recurrent neural networks for efficient language modeling. *Applied Soft Computing*, 79:354–362, Jun 2019. ISSN 1568-4946. doi: 10.1016/j.asoc.2019.03.057. URL <http://dx.doi.org/10.1016/j.asoc.2019.03.057>.
- [50] Yinchong Yang, Denis Krompass, and Volker Tresp. Tensor-train recurrent neural networks for video classification. In Doina Precup and Yee Whye Teh, editors, *Proceedings of the 34th International Conference on Machine Learning*, volume 70 of *Proceedings of Machine Learning Research*, pages 3891–3900, International Convention Centre, Sydney, Australia, 06–11 Aug 2017. PMLR. URL <http://proceedings.mlr.press/v70/yang17e.html>.
- [51] Jinmian Ye, Linnan Wang, Guangxi Li, Di Chen, Shandian Zhe, Xinqi Chu, and Zenglin Xu. Learning compact recurrent neural networks with block-term tensor decomposition, 2017.
- [52] Zichao Yang, Marcin Moczulski, Misha Denil, Nando de Freitas, Alex Smola, Le Song, and Ziyu Wang. Deep fried convnets. In *The IEEE International Conference on Computer Vision (ICCV)*, December 2015.
- [53] Song Han, Huizi Mao, and William J. Dally. Deep compression: Compressing deep neural networks with pruning, trained quantization and huffman coding, 2015.
- [54] Ilya Sutskever, Oriol Vinyals, and Quoc V Le. Sequence to sequence learning with neural networks. In Z. Ghahramani, M. Welling, C. Cortes, N. D. Lawrence, and K. Q. Weinberger, editors, *Advances in Neural Information Processing Systems 27*, pages 3104–3112. Curran Associates, Inc., 2014b. URL <http://papers.nips.cc/paper/5346-sequence-to-sequence-learning-with-neural-networks.pdf>.
- [55] Pierre Baldi. Autoencoders, unsupervised learning, and deep architectures. In *Proceedings of ICML workshop on unsupervised and transfer learning*, pages 37–49, 2012.

A Additional output

In this section, we illustrate the performance of the trained network on additional challenging test samples, in which the inputs exhibit noticeable heterogeneities. These samples are extracted from the test data set of the patient 0, patient 3, and patient 5.

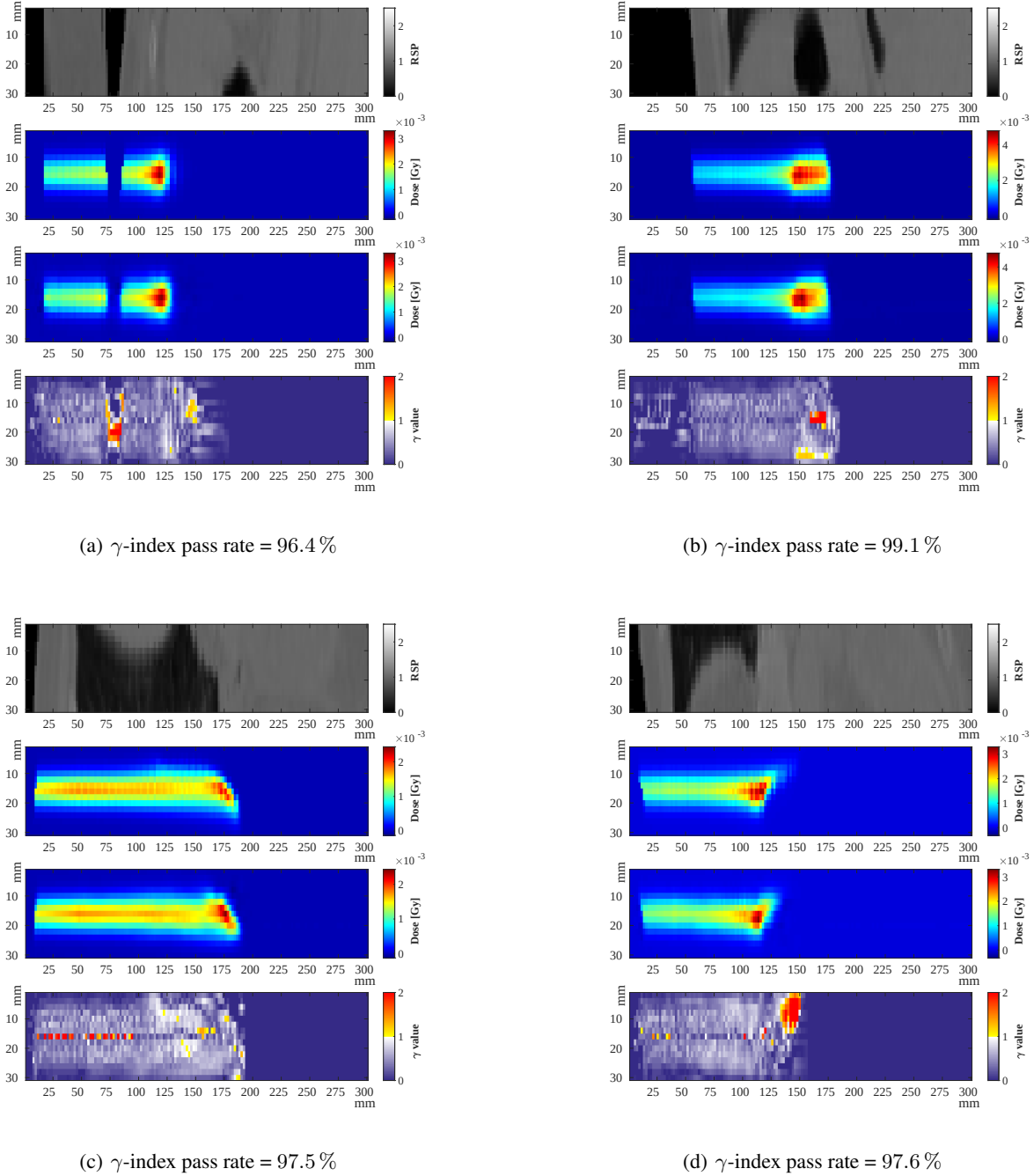
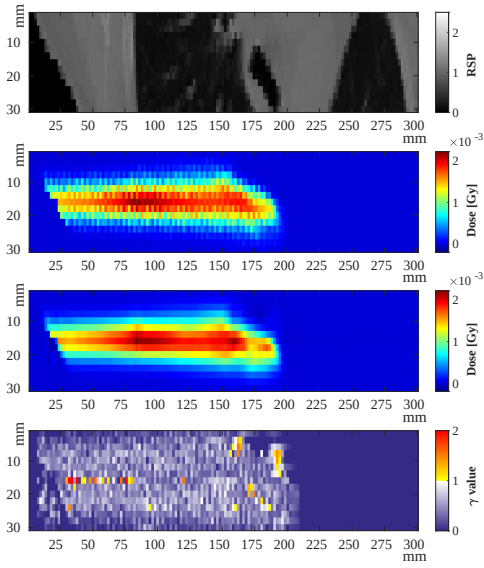
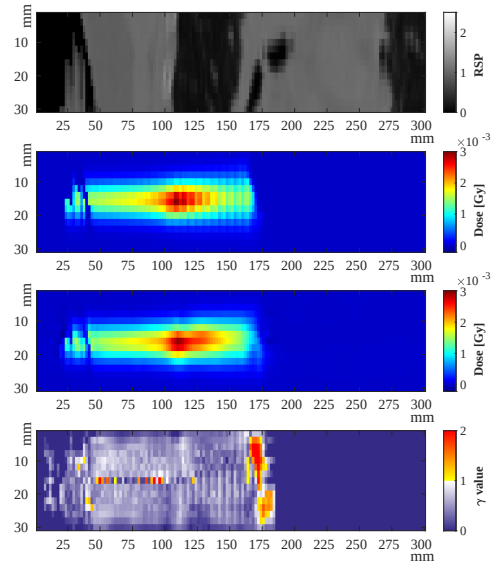


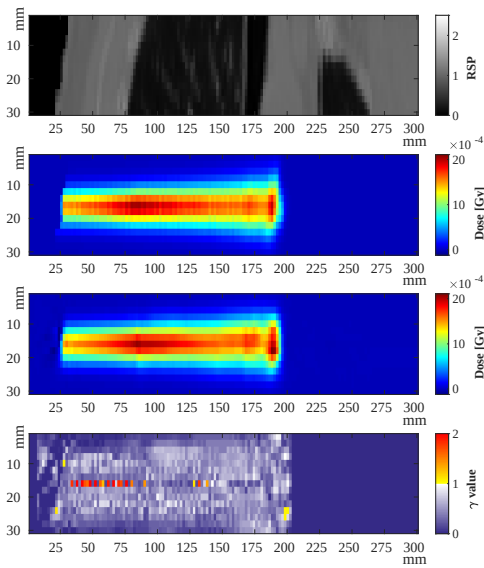
Figure 12: Dose estimation results for 4 test data from patient 0 ($E = 104.25$ MeV, γ -index criteria = $[0.5\%, 2$ mm]). The Subfigures follow the layout outlined in figure 11. Note that sample (a) has an air gap between the patient’s arm and chest (discussed in section 4).



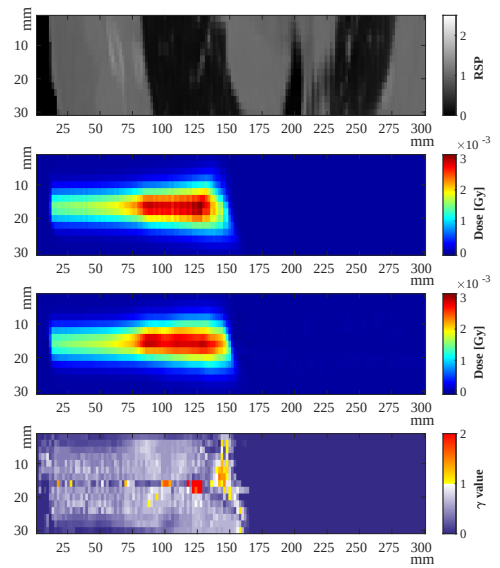
(a) γ -index pass rate = 97.8 %



(b) γ -index pass rate = 97.1 %

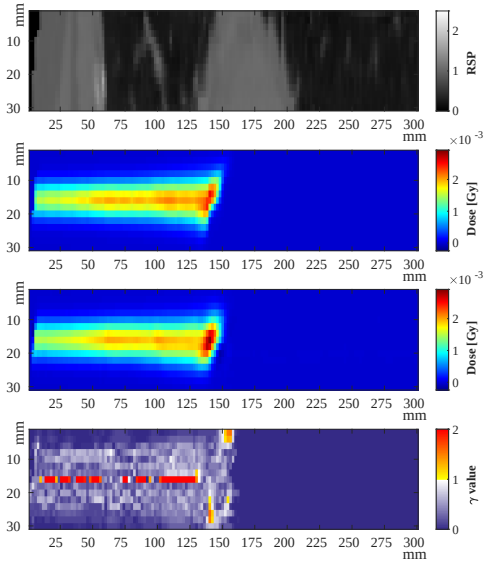


(c) γ -index pass rate = 98.3 %

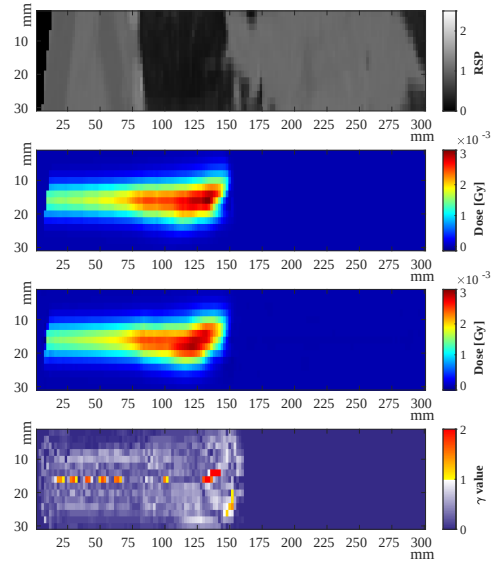


(d) γ -index pass rate = 98.7 %

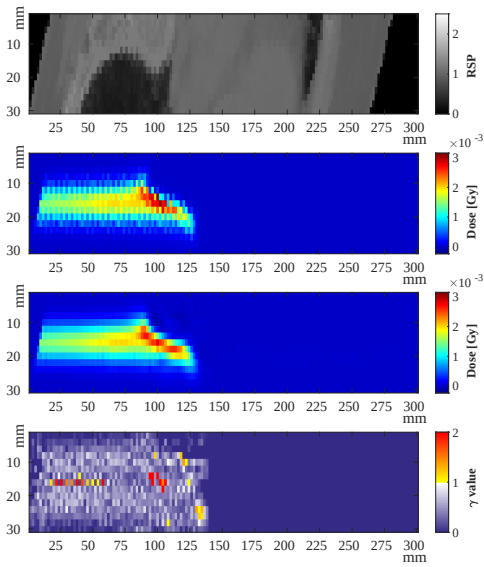
Figure 13: Dose estimation results for 4 test data from patient 0 ($E = 104.25$ MeV, γ -index criteria = [0.5 % , 2 mm]). The Subfigures follow the layout outlined in figure 11. Note that the aliasing effect in sample (a) is due to the cube extraction interpolation of oblique gantry angles.



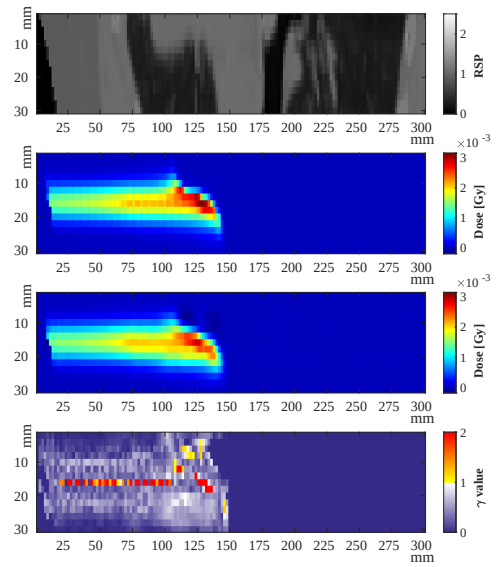
(a) γ -index pass rate = 98.1%



(b) γ -index pass rate = 98.4%

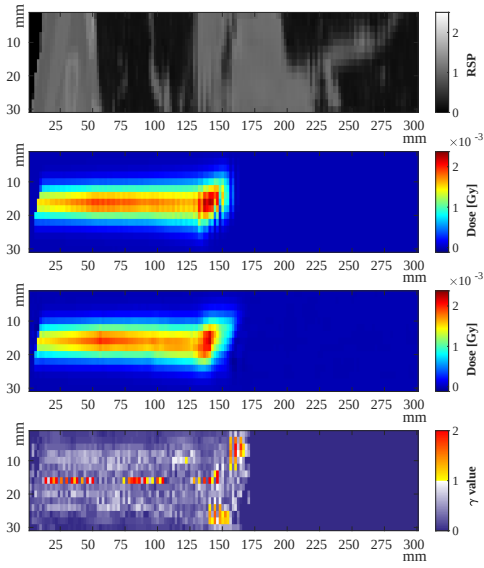


(c) γ -index pass rate = 98.6%

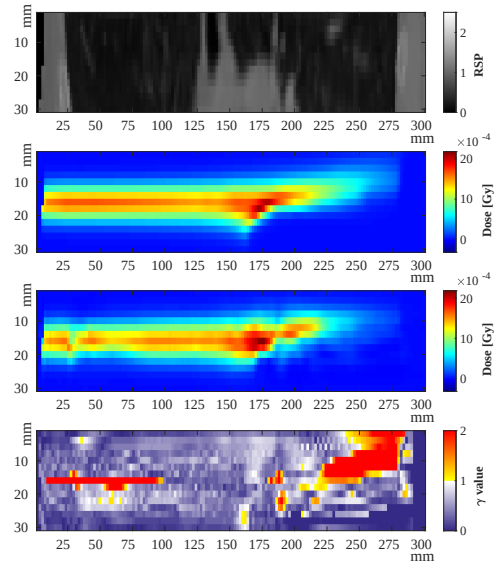


(d) γ -index pass rate = 98%

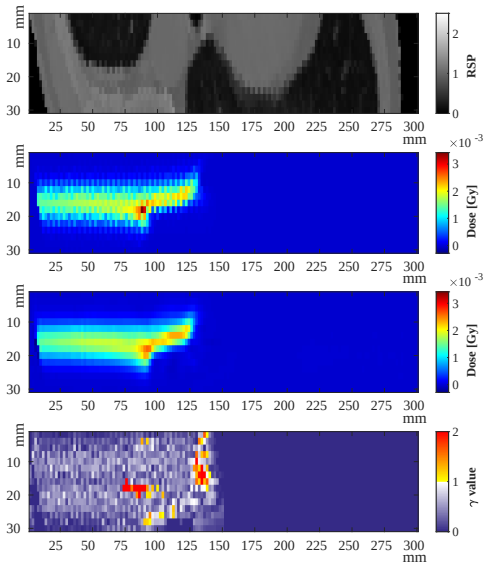
Figure 14: Dose estimation results for 4 test data from patient 3 ($E = 104.25$ MeV, γ -index criteria = [0.5%, 2 mm]). The Subfigures follow the layout outlined in figure 11.



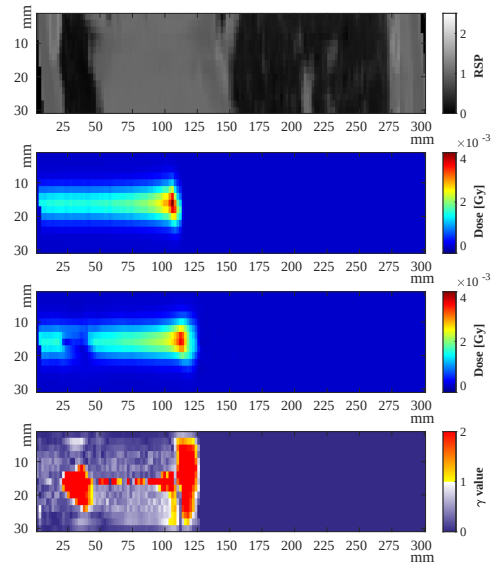
(a) γ -index pass rate = 98.2 %



(b) γ -index pass rate = 93.2 %



(c) γ -index pass rate = 97.5 %



(d) γ -index pass rate = 91.4 %

Figure 15: Dose estimation results for 4 test data from patient 5 ($E = 104.25$ MeV, γ -index criteria = [0.5 % , 2 mm]). The Subfigures follow the layout outlined in figure 11. Note that the network fails to distinguish between the lung and the air cavity in sample (d) due to the very low RSP value of the lung.